Geophys. J. Int. (2007) **171,** 244–258 doi: 10.1111/j.1365-246X.2007.03508.x

Validating tomographic model with broad-band waveform modelling: an example from the LA RISTRA transect in the southwestern United States

Teh-Ru Alex Song* and Don. V. Helmberger

Division of Geological and Planetary Sciences, Seismo Lab, Caltech, Pasadena, CA 91125*, USA. E-mail: alex@gps.caltech.edu*

Accepted 2007 May 25. Received 2007 April 12; in original form 2006 November 14

SUMMARY

Traveltime tomographic models of the LA RISTRA transect produce excellent waveform fits if we amplify the damped images. We observe systematic waveform distortions across the western edge of the Great Plains from South American events, starting about 300 km east of the centre of the Rio Grande Rift. The amplitude decreases by more than 50 per cent within array stations spanning less than 200 km while the pulse width increases by more than a factor of 2. This feature is not observed for the data arriving from the northwest. While the *S*-wave tomographic image shows a fast slab-like feature dipping to the southeast beneath the western edge of the Great Plains, synthetics generated from this model do not reproduce the waveform characteristics. However, once we modify the tomographic image by amplifying the velocity contrast between the slab and adjoining mantle by a factor of 2–3, the synthetics produce observed amplitude decay and pulse broadening. In addition to the traveltime delay, amplitude variation due to wave phenomena such as slab diffraction, focusing and defocusing provide much tighter constraints on the geometry of the fast anomaly and its amplitude and sharpness as demonstrated by a forward sensitivity test and snapshots of the seismic wavefield. Our preferred model locates the slab 200 km east of the Rio Grande Rift dipping 70°–75° to the southeast, extending to a depth near 600 km with a thickness of 120 km and a velocity of about 4 per cent fast. In short, adding waveform and amplitude components to regional tomographic studies can help validate and establish structural geometry, sharpness and velocity contrast.

Key words: body wave amplitude, delamination diffraction, finite difference, Rio Grande Riff, waveform modelling.

1 INTRODUCTION

Traveltime tomography has been one of the main tools in studying regional Earth structure. Standard practice for geodynamists is to convert these velocity anomalies into temperature and density and fit geophysical observables such as topography and gravity. Numerical studies have clearly shown significant variations in seismic velocity (Slack *et al.* 1994, 1996; Myers *et al.* 1998; Roth *et al.* 1999; Achauer & Masson 2002; Davis & Slack 2002; Gao *et al.* 2003; Tiberi *et al.* 2003), which has been used to map the temperature and composition in the mantle (Goes *et al.* 2000; Cammarano *et al.* 2003; Godey *et al.* 2004), infer the degree of partial melt (Hammond & Humpreys 2000; Takei 2000), and generate dynamic flow models driven by buoyancy variations mapped from seismic velocity anomalies (Forte & Perry 2000; Perry *et al.* 2003). However, tomographic models produced by smooth, damped inversions usually underestimate the amplitude and sharpness of the velocity structure and likely bias geophysical and geodynamic inferences. It is important to validate these tomographic models and propagate seismic waves through them and compare synthetic waveforms directly with observations. It enables us to amplify and sharpen these models and give a better estimate on the geometry and magnitude of seismic structures. Body waveform modelling has shown great success in understanding deep mantle structures (Wang & Wen 2004; Helmberger & Ni 2005; Ni *et al.* 2005; Song *et al.* 2005). However, it has seldom been used to test against regional tomography models and study lithospheric structure.

It is generally assumed that teleseismic body waves are simple enough to apply cross-correlation techniques in measuring traveltime anomalies. However, as we will show, these waves often display complexities and provide more information about local Earth structure near the recording site. We demonstrate how to examine the lithospheric structure beneath the eastern portion of the Rio Grande Rift in the southwestern US, one of the major continental rift zones in the world (Baldridge *et al.* 1991). To understand its origin and evolution, a recent PASSCAL experiment, LA RISTRA Transect, was operated in 1999–2001 to investigate seismic structures across

*Current address: Department of Terrestrial Magnetism, Carnegie Institution of Washington, NW Washington, DC 20015, USA. Email: asong@ciw.edu

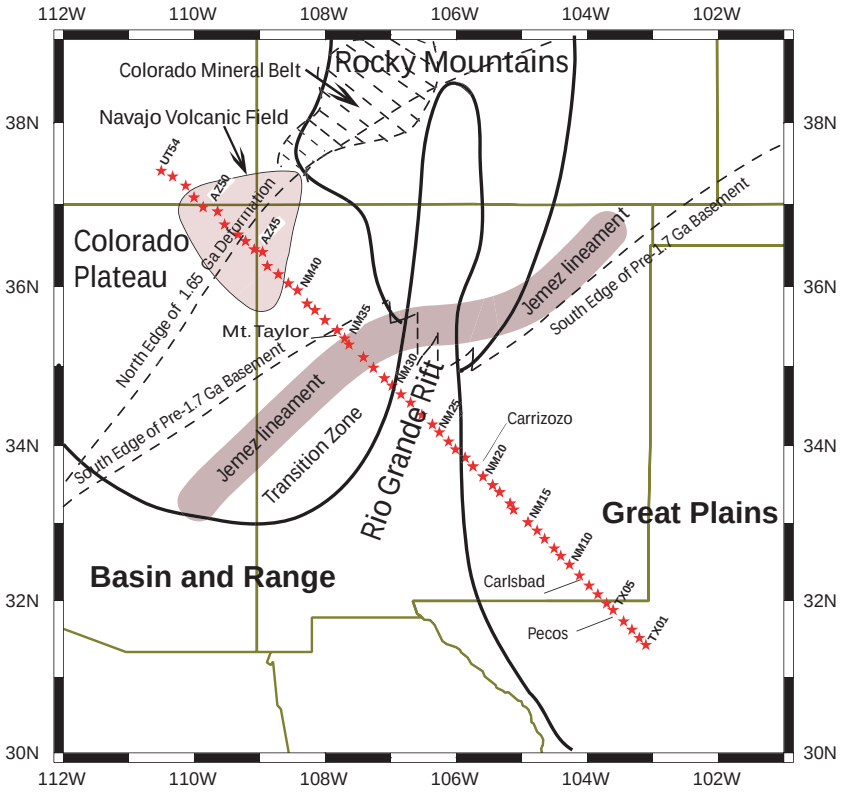

Figure 1. Geological settings at LA RISTRA Transect, southwestern United States (from Gao *et al.* 2004). The array (red stars) cuts across the Great Plains, the Rio Grande Rift and the Colorado Plateau and is aligned with great-circle paths from South American earthquakes.

the stable Great Plains, the Rio Grande Rift and the Colorado Plateau (Wilson *et al.* 2002, Fig. 1).

Using such a dense linear array, nearly 950 km long with 18 km spacing, enables the imaging of the lithospheric structure in great detail with body wave tomography (Gao *et al.* 2004), surface wave tomography (West *et al.* 2004a,b) and receiver function analysis (Wilson *et al.* 2005a,b). Gao *et al.* (2004) imaged a linear, southeast dipping slab-like fast anomaly under the western edge of the Great Plains, which is adjacent to the slow Rio Grande Rift (Fig. 2). Gao *et al.* (2004) interpreted it as a down-welling lithosphere produced by small scale convection. The velocity contrast between fast and slow regions reaches up to about 7 per cent in the upper 100 km but decreases at depth. West *et al.* (2004a) performed a surface wave inversion and found complementary results although the slab-like feature is less obvious in their model (Fig. 2). They also argued that there is a fast anomaly beneath the Great Plains extending at least to depths of 250 km, which is confirmed in a later study by joint inversion of body and surface waves (West *et al.* 2004b). These studies have performed standard resolution tests (checkerboard) to demonstrate the robustness of their results, but stop short of a true test by generating the wavefield.

While it is often considered that high attenuation is related to low velocity regions, which lowers amplitudes and increases pulse width, this data set suggests that it is not the main controlling factor. We observe systematic amplitude decays across stations located directly above the fast anomaly (e.g. NM07) and those above the transition region (e.g. NM15), whereas waveforms recorded at stations near the centre of the Rio Grande Rift (e.g. NM29) do not show obvious pulse broadenings and amplitude decays (Song 2006). It appears that wave propagational effects are playing a dominant role in producing waveform distortions and amplitude decays.

In this paper, we examine tangential SH broad-band waveform since *S*-wave anomalies typically are much stronger than *P*-wave anomalies. To demonstrate the usefulness of including waveform and amplitude information in improving seismic images, we focus first on the transition region from the Great Plains to the rift zone where we expect the largest velocity contrast to occur and waveforms to be heavily distorted. In particular, as we will show later, these waveforms are systematically distorted, broadened and their amplitude decreases accordingly. Instead of cross-correlation, we choose to pick arrival times, measure waveform amplitudes and use them as observables to compare with synthetic. We choose NM07 as the reference station because its waveform always appears narrower and simpler than those recorded at other stations toward the NW. Besides, its amplitude is often the largest in comparison to that recorded at stations to the SE. We then use the *S* waveform recorded at the reference station as the source wavelet to remove complexities generated from the earthquake source and near-source structure. We find it not critical to our analysis since we are primarily interested in modelling the pattern of changes in traveltime delays and amplitude decays. We then implement tomographic models into the 2-D finite difference calculations and compare synthetics against the observed waveforms. However, we find the synthetics too simple in waveform shape and inconsistent with the data. Simply amplifying velocity anomalies produced by traveltime tomography, we achieve a much better fit to the observed waveform complexities. We also perform a suite of synthetic tests on simplified models to demonstrate the usefulness of broad-band waveform and amplitude information in deciphering the location, geometry, and depth extent of dipping structures. We will further analyse *P* waveforms in a separate paper (Song & Helmberger 2007) and the joint results will provide important constraints on the physical state and composition

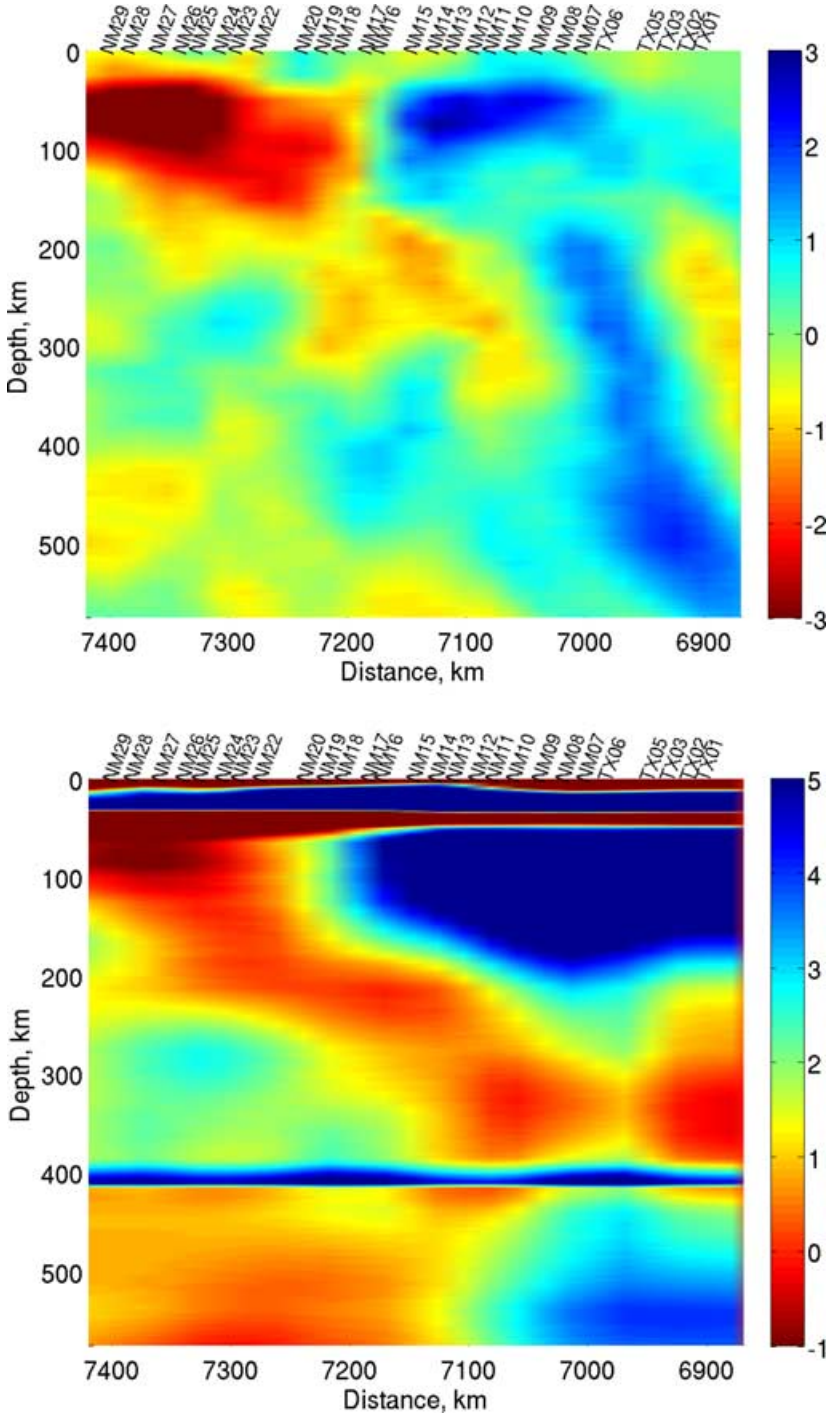

Figure 2. *S*-wave tomographic images beneath the array from body waves (upper panel) Gao *et al.* (2004) and surface waves (lower panel) (West *et al.* 2004a). A fast slab-like anomaly dipping to the southeast is imaged beneath the edge of western Great Plains by the body waves, which is not evident in the surface wave results. These models are plotted against the reference TNA model (Grand & Helmberger 1984).

of this interesting slab-like feature. Although other features shown in the tomographic image appear interesting as well, we will leave for future analysis.

2 WAVEFORM DATA

We first introduce broad-band waveform data from deep events beneath South America recorded by the array. It was configured to take advantage of the 2-D geometry with respect to South America events (Table 1). All the sections span about 2° from the Great Plains into the Rio Grande Rift. More precisely, stations NM07–NM18 are located directly above the slab-like feature shown in Fig. 2, although we do not know the true 3-D structure. We rotate the horizontal components to obtain the radial component along the great-circle path and corresponding tangential component.

We first present *P* and *SH* waveforms from event 990915 to the SE (Fig. 3). The bandpass filter used here and Figs 3 and 4 are chosen differently to present waveforms in consistency and accommodate

Table 1. Earthquake source parameter.

Event date	Longitude	Latitude	Depth	Strike	Dip	Rake	M_w
99/09/15	−67.37	−20.73	217.5	351	82	−70	6.4
99/11/30	−69.37	−19.01	138.2	354	81	−107	6.5
00/05/12	−66.85	−23.72	226.6	5	80	−96	7.1
00/04/23	−63.04	−28.41	607.9	171	88	−86	6.9
99/09/18	157.53	51.02	67.7	172	87	92	6.0

differences in data qualities. As shown in Fig. 3, the amplitude of *S* waves decreases very rapidly in this range with a reduction over 50 per cent. The waveforms also become broader with less high frequency content. However, such a systematic behaviour is not seen in the record section from event 990918 arriving from Kamchatka to the NW (Fig. 3).

We check possible shallow receiver complexities as the causes by examining the vertical and radial components of the *P* wave. However, the similarity of *P* waves in both vertical and radial components do not support such an argument, while the tangential component is nearly zero, indicating wave field separation into (P-SV, SH) motions (Song 2006). The observed waveform distortion and amplitude variations are consistent regardless of the location and the depth of several events to the SE suggesting receiver-side structure effects (Fig. 4). In addition, other phases such as *sS* waves and *ScS* waves also show similar patterns (Fig. 4).

In order to remove the complexities introduced by individual earthquake sources, we deconvolve the source wavelet from the raw seismogram to generate an uniform data set. Since the great-circle paths to these stations differ by less than 2°, the directivity effect on the source–time function in this narrow range is probably very similar. Because we observe systematic waveforms broadening for all events we have analysed, we decided not to use the stacked *S* waveform as the source wavelet. As discussed earlier, we adopt the simplest and narrowest *S* waveform recorded at station NM07 as the source wavelet for deconvolution processes. We apply a regularized filtered algorithm to stabilize the deconvolution (Jain 1989) and the deconvolved waveform typically has a dominant period of 6–8 s. All the deconvolved record sections from four events to the SE display consistent results where the peak amplitude of the *S* wave decreases from station NM07 to NM18 by a factor of 2–3 and the pulse width is broadened by a factor of 2–3, independent of the source depth and epicentral distance (Fig. 5).

The consistency of these data sets strongly suggests that receiver-side structure plays a predominant role in producing such systematic waveform distortions and amplitude decays. We will attempt to model these features with a 2-D finite-difference code (Vidale *et al.* 1985; Helmberger & Vidale 1988; Vidale 1988). Although

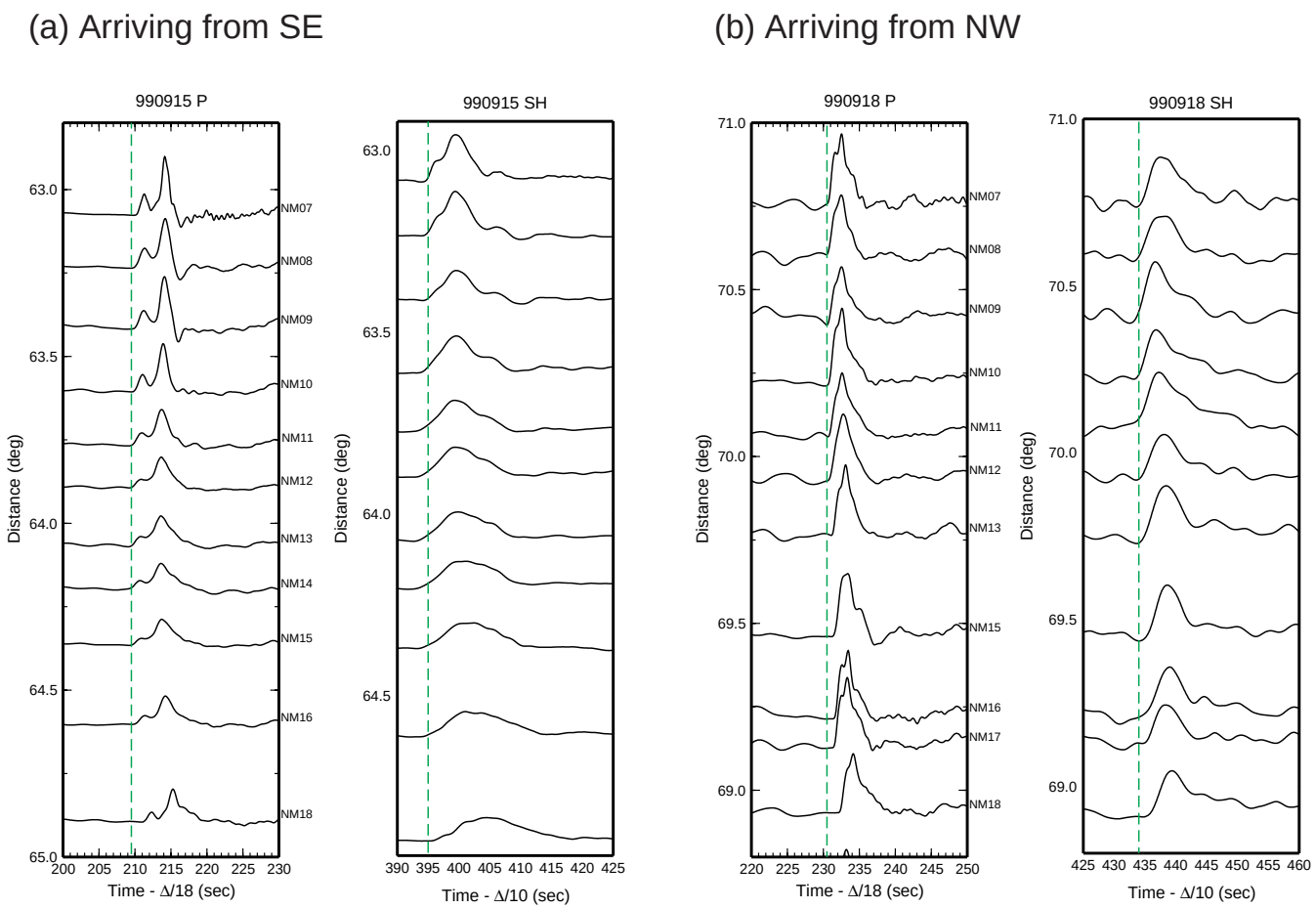

Figure 3. *P* and *SH* displacement record sections for event 990915 from (a) South America (SE) and event 990918 (b) Kamchatka (NW). The absolute amplitudes of *P* and *S* waves both reveal significant decreases across the range of distances while their pulse widths become much broader at stations directly above the western side of fast slab in (a). Although the signal-to-noise ratio is lower for the record sections shown in (b), no significant amplitude decrease or waveform broadening is observed. The data shown in (a) and (b) are bandpass filtered with corners at 0.02 and 2 Hz for *P* waves, 0.02 and 1 Hz for *S* waves, respectively.

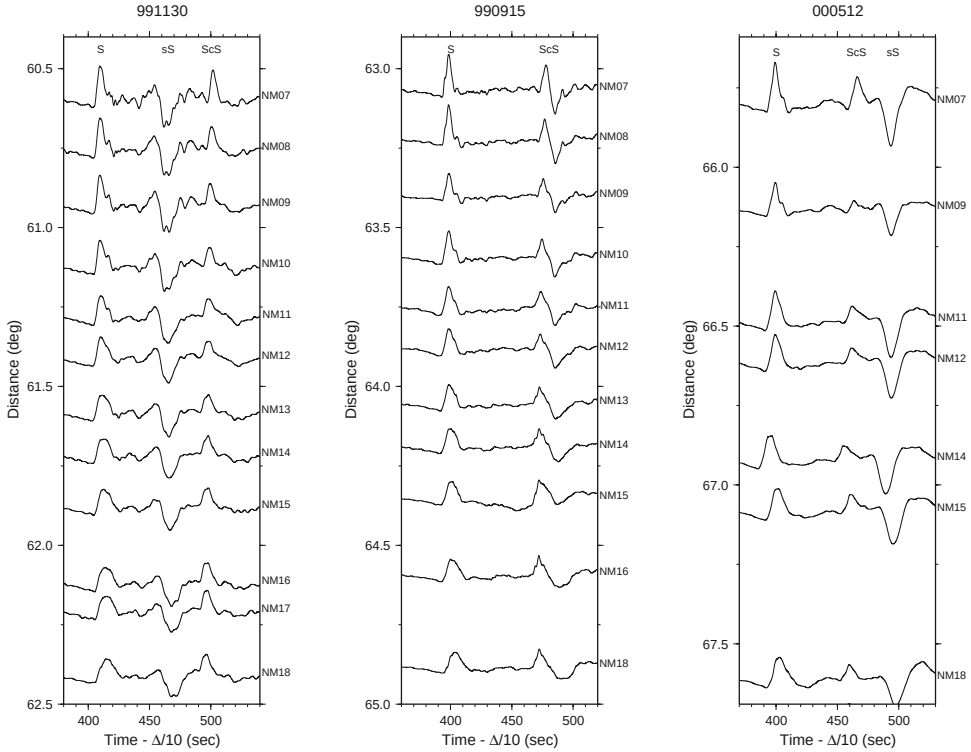

Figure 4. Tangential displacement record sections of four events from South America; from left to right: 990915, 991130, 000512 and 000423. All four record sections show systematic amplitude decrease and waveform broadening over the stations NM07–NM18 interval. Note that not only the *S*, *sS* and *ScS* waves reveal similar observational features. The data are bandpass filtered with corners at 0.012 and 2 Hz.

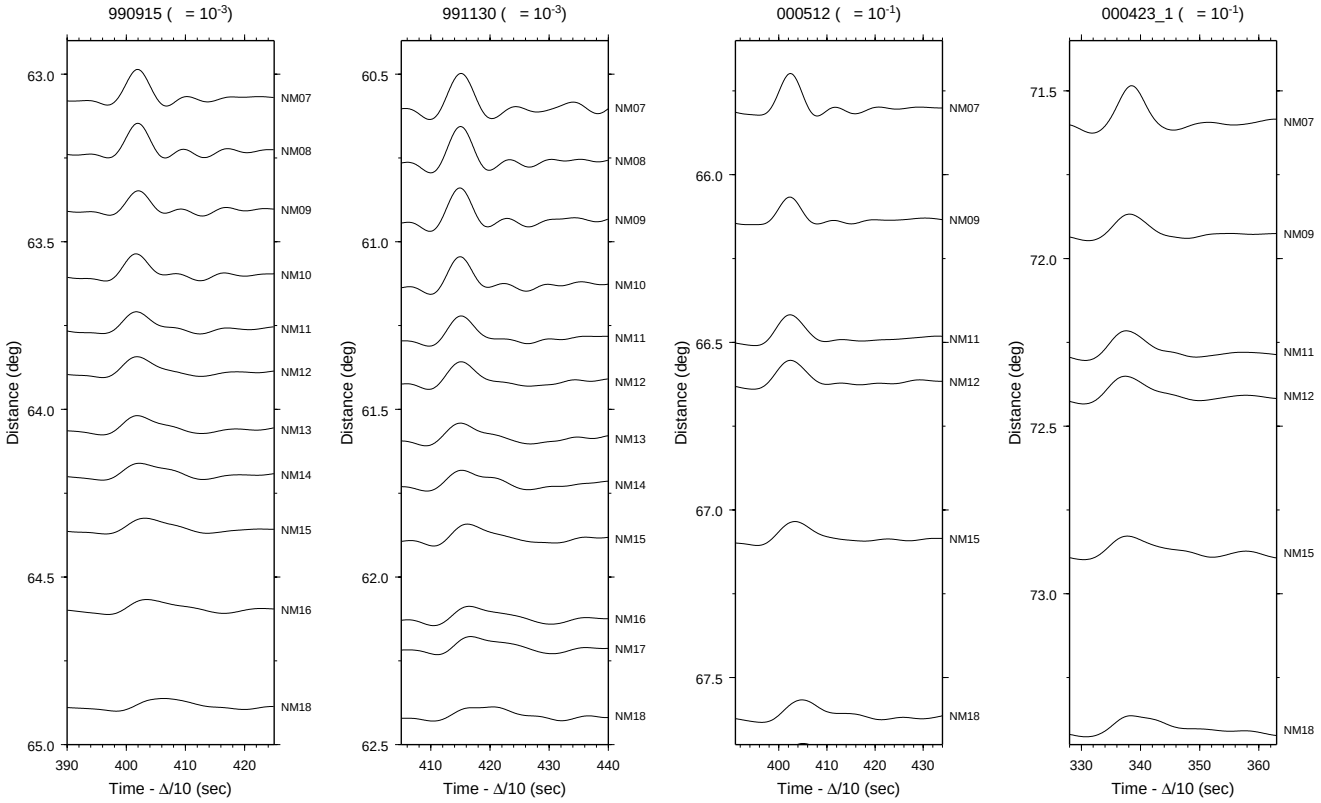

Figure 5. Record sections of deconvolved *SH* waveforms. From left to right: 990915, 991130, 000512 and 000423. The amplitude decreases by more than half from station NM07 to station NM18, while the pulse width increases by more than a factor of 2. The dominant period of these deconvolved waveforms is about 6–8 s.

only four events are analysed in this paper, we will show indeed that our preferred model can give promised fits to these data sets at multiple frequency bands and predict satisfactory results against data sections from events of different distances and depths.

3 FINITE DIFFERENCE MODELLING

The finite difference code has been used to investigate the upper-mantle triplication (Song 2006) and core mantle boundary structure (Song *et al.* 2005) and it has been successfully bench-marked against semi-analytic codes such as 1-D reflectivity (Song 2006) and 2-D WKM (Song *et al.* 2005). In the following simulations, we adopt a grid spacing of 1.6 km and a time step of 0.077 s to ensure convergence and accuracy at periods of 3.0 s and longer. We set the grid boundaries far enough away from the source and receivers to avoid the interference of reflections with the *S* wave of interest. A Butterworth filter with corners at 0.01 and 0.2 Hz is applied to both the data and synthetics. To examine the effect of long wavelength mantle structure on the waveform broadening and amplitude decay, we have computed synthetics based upon the global

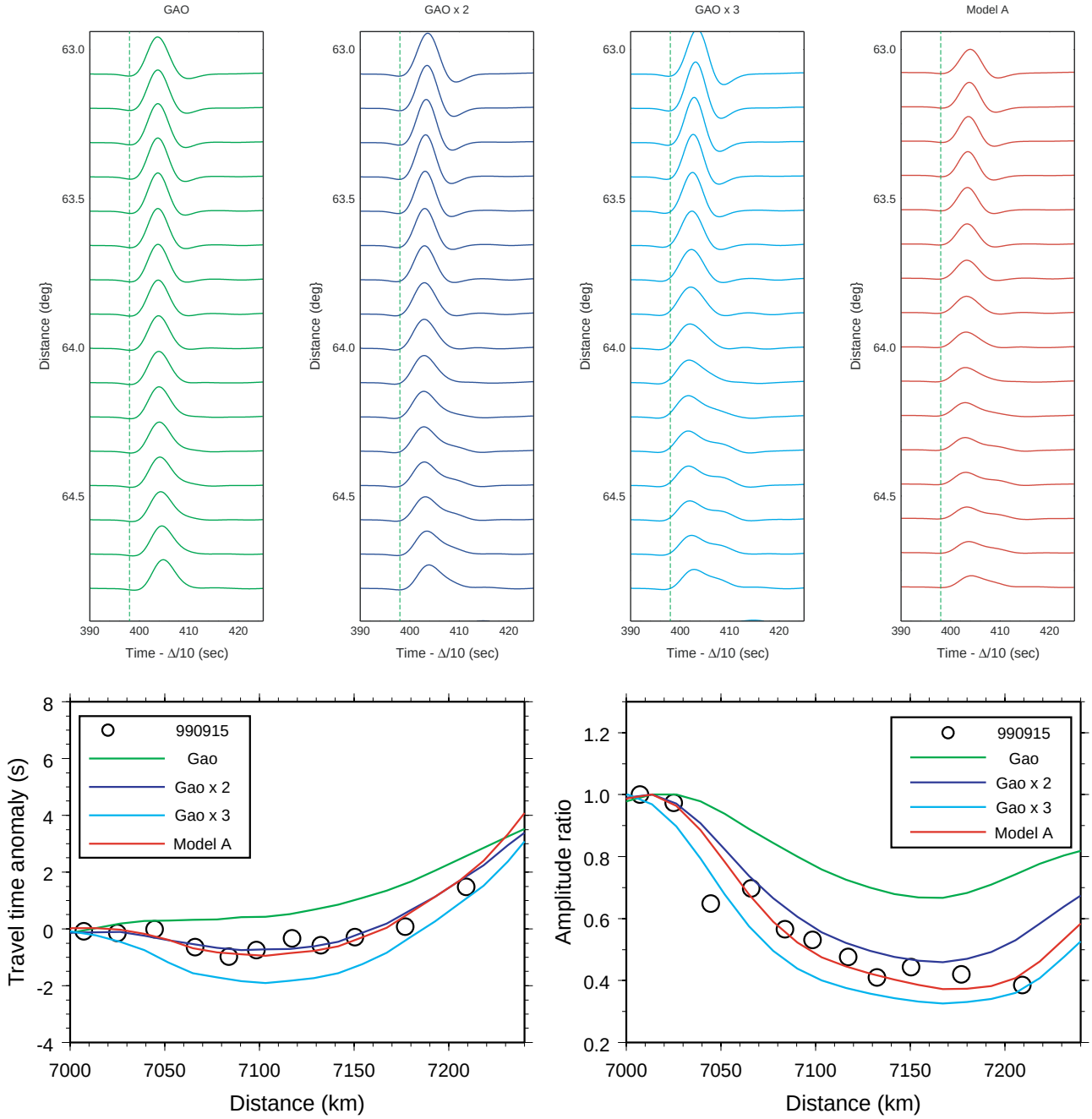

Figure 6. FD synthetics (upper panel), traveltime delays and amplitude ratio (lower panel). Finite difference synthetics are computed using the *S*-wave tomographic image (Body waves) constructed beneath the array by Gao *et al.* (2004). The velocity anomaly in the tomographic image is amplified by one, two and three times to compute synthetics in the left three columns. To fit both traveltime delays and amplitude ratios, model A is constructed by amplifying the fast anomaly by two and slow anomaly by four (right-hand column). The lower left-hand panel displays the comparison of measured traveltime delays and predictions. The lower right-hand panel shows the comparison of measured amplitude ratios and predictions. Traveltime delays and amplitude ratios are measured relative to reference station NM07.

tomographic model by Grand (2002). We find that the long wavelength mantle structure does not produce any notable amplitude decay in the record sections of all four events we currently studied (Song 2006). However, if sharp features are present in the source region that are not in Grand's model, we would expect to see differences in the data associated with sampling in the four observed sections. Since the amplitude pattern is stable, we suppose that it is caused pre-dominantly by the receiver structure.

To examine the effect of receiver-side structure on broad-band waveforms, we propagate the waves through the 1-D TNA model (Grand & Helmberger 1984) from the source to the receiver with the 2-D regional tomographic models (Gao *et al.* 2004; West *et al.* 2004a) embedded locally beneath the stations. We generate synthetic waveforms and present traveltime delays and amplitude ratios relative to reference station NM07. The data and synthetics are both filtered at frequency band of 0.01–0.2 Hz. Since these waveforms are not similar and very different in pulse width, we choose not to cross-correlate them but pick the timing of the first swing in filtered waveforms to measure traveltime delays, which is similar to Gao *et al.* (2004)'s approach. The amplitude is then computed by taking the envelope of the *S* wave and measuring its peak. We first examine the data of event 990915 at the range of 63°–65° and synthetics computed from 2-D tomography models by Gao *et al.* (2004). The synthetics are very simple and their amplitude does not decay with distance as much as the data (Fig. 6). In addition, the predicted traveltime anomalies vary smoothly across the range (Fig. 6).

Considering the smoothing and damping made in most inversion procedures, we then simply amplify the magnitude of the velocity anomalies and recompute the synthetics. As introduced earlier, we focus on the waveform phenomena within a relatively small region where velocity varies rapidly. This simple procedure is useful in amplifying velocity anomalies in these transition regions from fast to slow. However, such a process could deteriorate the fit to traveltime delays outside the transition region of interest. To quantify the quality of fit, we compute misfits of traveltime delays and amplitude decay between data and synthetics, respectively. The misfit is defined as the L2 norm of the differences in traveltime and amplitude between data and synthetics. Overall, the result is satisfying in that the synthetics start revealing similar waveform distortion and amplitude decay as displayed in the data (Fig. 6). Our preferred model A is constructed by amplifying the fast anomalies by two times and slow anomalies by four times such that it can explain traveltime delays and amplitude decays simultaneously (Table 2).

It is well known that teleseismic body wave traveltime tomography has better resolution laterally than vertically. We have further tested possible vertical smearing of the tomography model. In this case, we only implement the top 250 km of the velocity model into the FD calculation. This exercise shows that, with an unrealistic amplification factor of 8, we then are able to explain the observations (Song 2006). However, such a model with 50 per cent velocity contrast is physically unlikely. In addition, this approach of amplifying anomalies did not work so well with the surface wave tomography model (West *et al.* 2004a). Even if we amplify the velocity perturbation in the mantle, the synthetics do not show similar waveform distortion and the amplitude decay is unsatisfactory (Song 2006). Furthermore, we were not able to fit the traveltime and amplitude simultaneously. As we expected, the surface wave derived tomography models do not capture the small-scale variation in the upper mantle and probably too smooth, especially in cases where structures exhibit rapid lateral variations. More importantly, the fast dipping anomaly is essential in producing these observations.

Table 2. Misfit of events 990915, 991130, 000512 and 000423.

Event 990915	Gao	Gao×2	Gao×3	Model A
Misfit-Time	3.443	0.806	2.963	0.868
Misfit-Amp	0.808	0.307	0.298	0.219
Event 991130				
Misfit - Time	2.485	1.686	4.934	2.352
Misfit - Amp	0.997	0.421	0.165	0.197
Event 000512				
Misfit - Time	1.380	1.325	3.809	1.616
Misfit - Amp	0.612	0.251	0.334	0.229
Event 000423				
Misfit - Time	2.670	0.868	1.953	0.906
Misfit - Amp	0.765	0.342	0.280	0.279

Before evaluating our preferred model against record sections of other events, we also compute traveltime delays in the frequency range of 0.03–0.1 Hz, which was the frequency range used by Gao *et al.* (2004) to construct tomographic images. We find that their model indeed explained traveltime delays a lot better at longer period (Fig. 7, Table 3). However, our preferred model A can fit the data slightly better at longer period but also explain data at shorter period (Fig. 7, Table 3) very well. When we convolved the source wavelet with synthetics of our preferred model A, the data and synthetics were compatible in amplitude variation, traveltime delay, and waveform distortion (Song 2006).

To further demonstrate the consistency of our model A, we generate synthetics for other three events at the distances of 60.5°–62.5° (event 991130), 65.8°–67.8° (event 000512) and 71.5°–73.5° (event 000423), using the same procedure to predict traveltime delays and amplitude decays. We obtain similar results with amplification factors of 2–3 while the traveltime delays and amplitude variations are reasonably well reproduced by model A (Figs 8 and 9, see also Table 2). These results confirm the local nature of the anomalous structure. Other tested models are not favoured because of the inability to explain the traveltime and amplitude simultaneously. For instance, model Gao × 3 explains the amplitude decays of event 000423 well. However, it produces a large misfit in traveltime delays (Table 2). Model Gao × 2 explained the traveltime delays well for event 991130, but it produces a large misfit in explaining amplitude data.

As pointed out by Vidale (1987) and Cormier (1989), source-side slab diffraction/multipathing causes waveform distortion recorded teleseismically, such as *S* and *ScS*, and also causes focusing and defocusing at teleseismic distances (Vidale 1987; Cormier 1989; Weber 1990; Sekiguchi 1992; Perrot *et al.* 1994; Zhou & Chen 1995). Such waveform effects and amplitude perturbation due to the high-velocity slab have often been used to constrain the geometry and depth of the slab near the source side. However, in this study, we focus on the slab structure near the receiver side probed by incoming teleseismic waves (Bostock *et al.* 1993). The multipathing from the SE side of slab (slow-to-fast boundary) magnifies the amplitude of the waveform (Fig. 10). Such an amplification is analogous to the upper-mantle triplication where two branches crossover, except the velocity jump is not horizontal but nearly vertical (Song & Helmberger 2006). In addition, this dipping feature produces a distorted wavefield which can be easily seen in the snapshots of wave

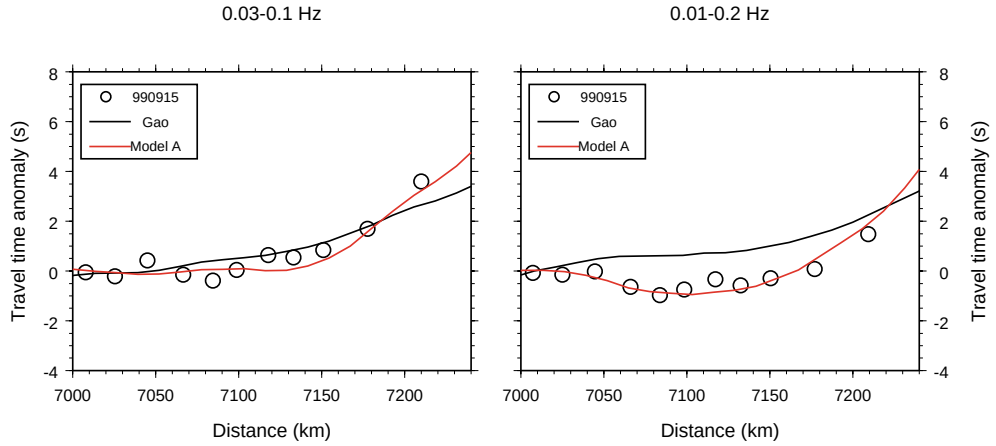

Figure 7. Traveltime delays computed at two frequency ranges. The panel on the left displays results at longer periods of 0.03–0.1 Hz used in Gao *et al.* (2004) study and the right-hand panel shows results at periods of 0.01–0.2 Hz.

Table 3. Misfit of traveltime delays.

Model	Gao	Model A
Misfit (0.03–0.1 Hz)	1.740	1.116
Misfit (0.01–0.2 Hz)	3.443	0.868

propagation along the slab structure (Fig. 11), where the wavefront is more advanced inside the high velocity slab and finally splits apart. It also creates long period energy between the two arrivals evident in the data (Figs 10 and 11).

In short, it is clear that receiver-side slab-like structure indeed plays a dominant role in producing observed waveform complexities and amplitude changes across the western Great Plains and the Rio Grande Rift. We show that he slab-like velocity anomaly probably exists as displayed in the tomographic model. However, based on our modelling, the average velocity contrast between the fast slab-like feature and the adjoining mantle is about 4 per cent down to nearly 600 km.

4 IDEALIZED MODEL SENSITIVITY: SLAB THICKNESS AND GEOMETRY

We have demonstrated above that the combination of travel-time delays and amplitude patterns provide strong constraints on

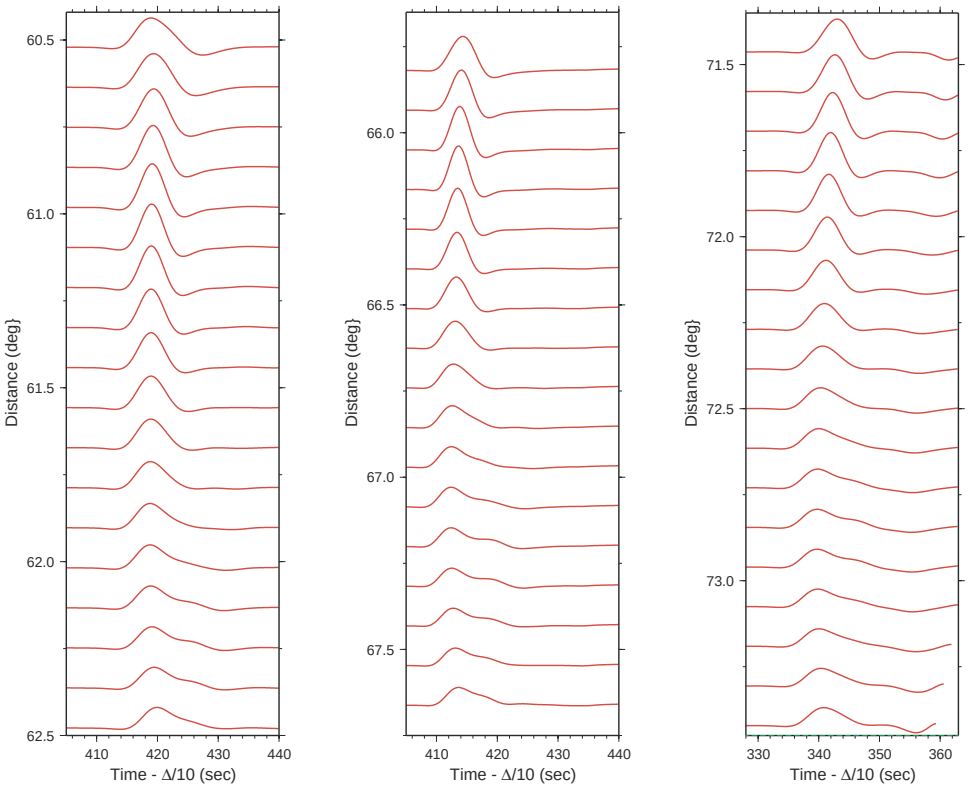

Figure 8. Finite difference synthetics computed using amplified tomographic image model A for other three events from South America. All synthetic record sections show comparable waveform distortions observed in the data (Fig. 5).

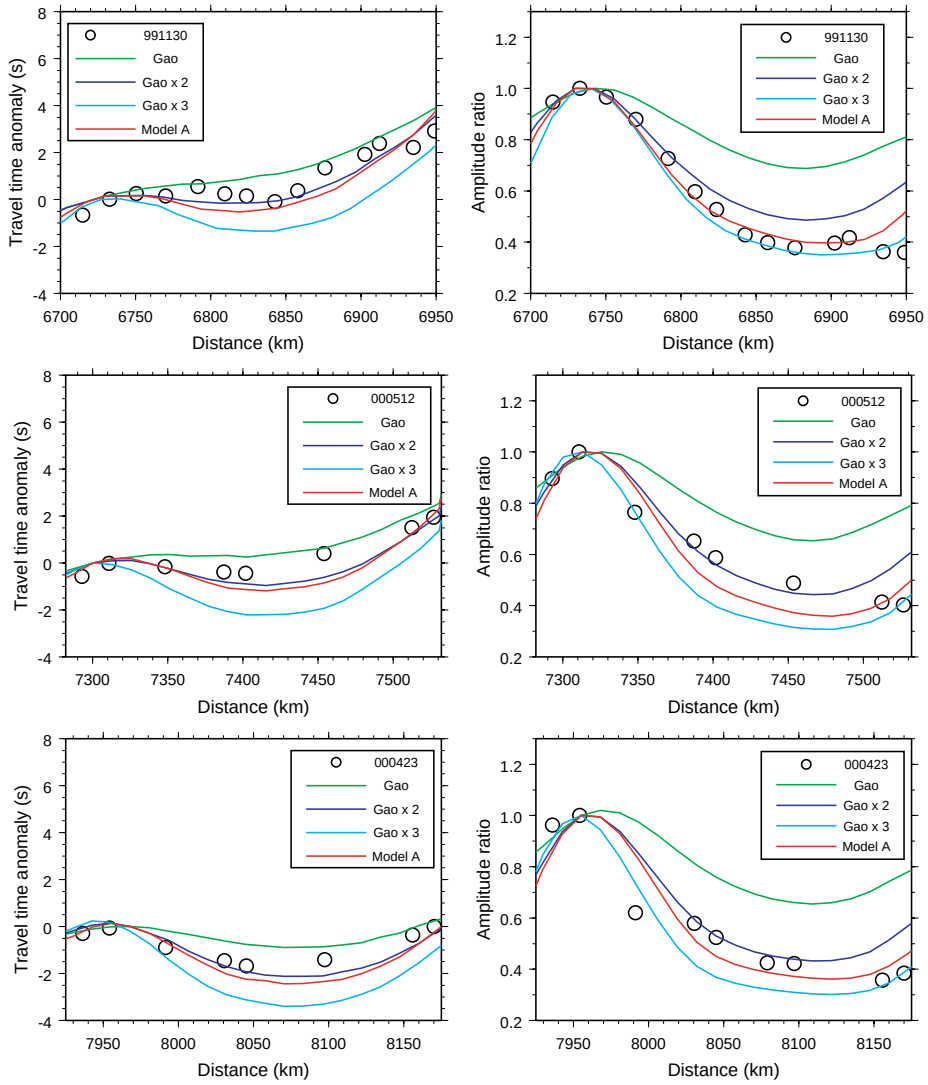

Figure 9. Traveltime delays and amplitude ratio computed for the three events displayed in Fig. 8. In general, model A predicted nice results against these data sets at different ranges (see also Table 2).

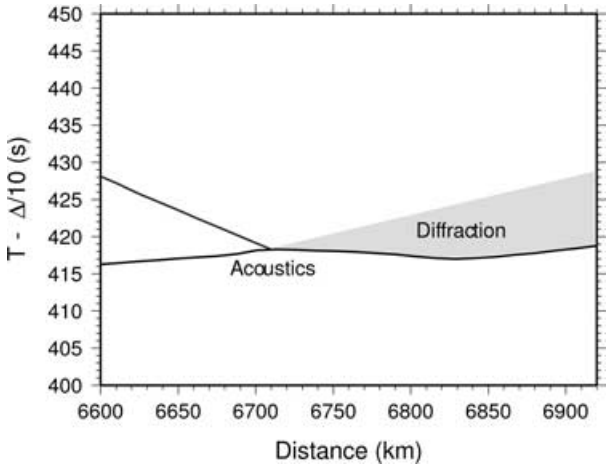

Figure 10. Schematic traveltime versus distance plot. Multiple branches are shown at shorter distance to the SE and form a caustic near 6700 km, where slow-to-fast transition occur. Diffraction energy is shown in grey to the NW representing waveform broadening observed in the observed record sections.

upper-mantle structure. However, it is difficult to investigate uniqueness given the complexity of model A. To appreciate the essential features of this model, we conduct a sensitivity experiment where Gao's model is idealized to a few parameters (Fig. 12). We perform tests with various combinations of parameters as given in Table 4, which includes possible trade-offs between the depth of the slab and its velocity perturbation.

We find that the amplitude is the smallest near the far-side the slab (NW) and the largest near the near-side of the slab (SE), but within the slab (Fig. 13). While the largest amplitude is sensitive to the width and dip of the slab, the amplitude decay rate with distance primarily depends on the thickness of the slab, where the wider the slab, the lower the decay rate. If we fix the dip and the width of the slab but change its depth extent, we find that the amplitude starts to increase again after passing the far side of the slab (Fig. 13) and begins to form another amplitude plateau. This amplitude plateau and the amplitude maximum at near-side of the slab (SE) produce an amplitude shadow zone whose width is very sensitive to the depth of the slab (Fig. 13). The deeper the slab, the wider the amplitude shadow zone. In other words, a deeper slab is more effective in defocusing the energy over a wider range than a shallower one.

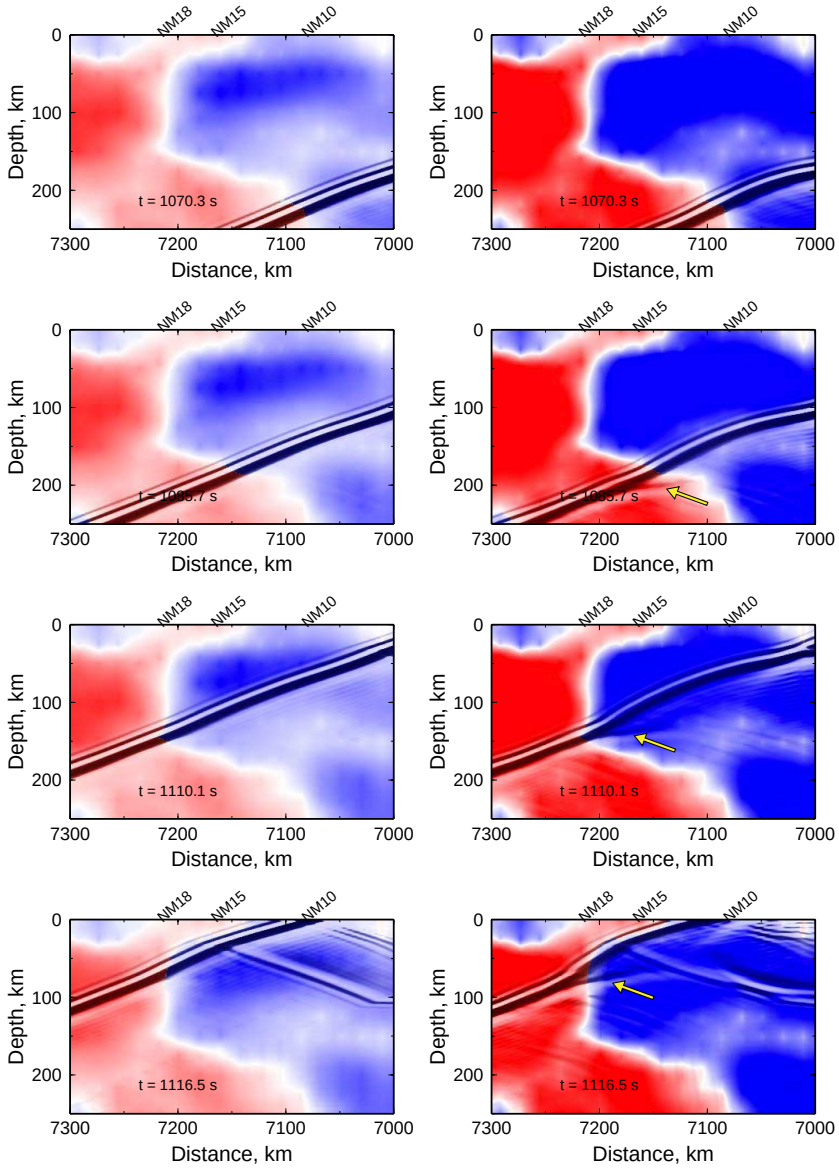

Figure 11. Finite difference snapshots for the original tomographic model (left-hand panels) compared with the amplified tomographic model (right-hand panels). The wavefront becomes much more distorted in the amplified model than the original model at time 1070.3 s. About 15 s later, the wavefront is starting to break (yellow arrow) and becomes separated into two for the amplified tomographic image. The broken wavefront is separated even more through continuous propagations along the velocity boundary. Only the top 250 km is presented with background image of velocity anomaly (±3 per cent). The location of station NM10, NM15 and NM18 is indicated for reference. For visualization purpose, the derivative of the wavefield is overlaid on top of the velocity anomaly to show the interaction between the wavefield and 2-D medium.

We can draw analogy from passing a wave through a distant, fast anomaly where wavefront distortion is over a much wider range (figs 9 and 10 in Hung *et al.* 2001). We find this feature particularly useful in eliminating the trade-offs between slab depth and its velocity anomaly.

We also test an extreme case with no slab but a fast-to-slow transition in the top 200 km. In this case, we consider possible vertical smearing in the tomographic image that produces an artificial slab-like feature. We still observe the amplitude decay associated with the diffraction along the boundary, but there is no amplification as seen close to the near-side (SE) (Fig. 13). In addition, the amplitude focusing and defocusing vary rapidly at a much shorter scale. If we add a low velocity zone in the top 200 km near the far-side of the slab to simulate the slow rift zone imaged by the tomography, it only modifies the amplitude pattern beyond the far-side of the slab. Finally, we examine the degree of amplitude decay due to the slab diffraction, which clearly depends on how strong the velocity anomaly is. In general, a strong velocity anomaly produces severe diffraction, defocusing and amplitude changes (Fig. 13), although it also depends on the incident angle of teleseismic waves and the dipping angle of the slab. However, such trade-offs can be reconciled if the traveltime anomaly is simultaneously analysed. In summary, the amplitude variation provides fairly good constraints on the location, geometry, depth extent of the slab-like anomaly and its amplitude. It provides complementary information beyond the traveltime data in resolving deep structure.

Based on these sensitivity tests, we produce a simplified model for the slab near the Rio Grande Rift to explain the data (e.g. event

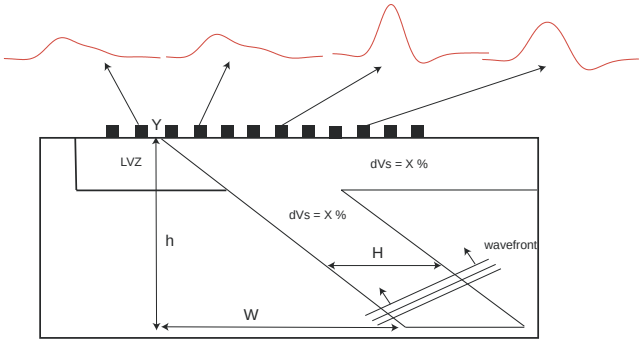

Figure 12. Slab diffraction and forward modelling setup. The waveform is narrow and amplified after crossing the eastern side of the slab. Just beyond the western side of the slab where fast-to-slow transition occurs, the waveform is much broadened and the amplitude is decreased due to waveform multipathing. Toward the west, the multipathing is less obvious and the waveform will start to become a simple pulse again. The slab is defined as a dipping layer *X* per cent fast than the surroundings. The dipping of the slab is defined by the depth h and the horizontal shift *X*, while the width of the slab is H. The western tip of the slab is defined at the point *Y* on the surface. A −3 per cent low velocity layer, 150 km thick is added adjacent to the slab in certain cases (see Table 4).

Table 4. Sensitivity test slab parameters.

No.	*W* (km)	*H* (km)	*h* (km)	*X* (per cent)	LVZ	*Y* (km)
I.A	150	100	575	6	no	7100, 8200
I.B	150	100	575	4	no	7100, 8200
I.C	150	100	575	2	no	7100, 8200
I.D	150	100	480	7	no	7100, 8200
I.E	150	100	384	9	no	7100, 8200
I.F	150	100	200	17	no	7100, 8200
I.G	150	100	575	6	yes	7100, 8200
II	250	100	575	6	no	7100, 8200
III	150	200	575	6	no	7100, 8200

991130). This model is built to mimic the tomographic image and fit the data through a systematic search of model parameters (Table 5). As a result, we are able to generate models which can reproduce the amplitude decay and traveltime anomaly (Fig. 14). We can fit the amplitude decay with a 120 km wide, 6 per cent fast slab dipping 80° to the southeast and reaching 575 km depth (Model SD-1), but it fails to explain the traveltime anomalies (Fig. 14, Table 6). Model SD-2 consists of a 3.75 per cent fast slab dipping 70° to the southeast. This model is able to fit the amplitude and traveltime anomaly simultaneously. We find that model SD-4 can also fit the amplitude decay well with a 4.5 per cent fast slab dipping 75° to the SE, although it slightly deteriorated the fit to traveltime delays (Table 6). Model SD-3 consists of 4.5 per cent fast slab reaching 380 km depth. It explains the traveltime delays reasonably well, but the amplitude increases much faster than the data behaved near the far-side of the slab, whereas the width of the amplitude shadow zone is too narrow (Fig. 14), which suggests that the slab is likely too shallow. As illustrated in previous sensitivity tests and model SD-3, the depth extent of the slab-like anomaly has to be deeper than 480 km to fit the width of amplitude shadow zone. Using both traveltime and amplitudes, we can mostly eliminate trade-offs between the geometry of the slab-like anomaly and its amplitude.

Modelling slab diffraction and defocusing pattern also provide tight control on the NW boundary of the slab. In short, the slab-like anomaly imaged by Gao *et al.* (2004) is amplified to explain waveform multipathing and diffraction. Our preferred model has a 3.8–4.5 per cent fast slab of 120 km thickness dipping at an angle of 70°–75° and reaching the depth near 570 km (Fig. 14). Also, the slab feature is shifted eastward from the centre of the Rio Grande Rift zone by 200 km.

5 DISCUSSIONS

In this section, we would like to first briefly discuss some issues regarding to the cross-correlation technique and how the amplified model does to other type of data, such as surface waves. As shown in previous section, there is little variation in traveltime from station NM07–NM15 while large delays occur beyond NM15. If we apply cross-correlation technique for these broadened waveforms, it would produce more delays for stations to the NW because the pulse broadening would shift the measure. We would expect a smooth timing change across these stations rather than an abrupt one, whereas the model constructed from these measures is potentially smooth. However, the details should be explored systematically in the context of ray-based traveltime tomography and finite-frequency tomography independently.

Although the amplified model explains the waveforms and amplitude better than the original model, we expect the new model would not effect surface waves very much because they travel horizontally crossing both fast and slow anomalies while the wavelength for surface waves is much longer than that of body waves. West *et al.* (2004b) have demonstrated that lateral variations mapped by body waves can be easily accommodated in surface waves tomography.

It is not surprised that a damped, smooth inversion would underestimate the true anomalies. However, the large amplification factor of slow anomalies (four times) used in our preferred model A is likely due to the fact that body waves are more sensitive to the fast anomalies and it is more difficult to see the slow anomalies. In particular, finite-frequency effect and wavefront healing (Hung *et al.* 2001) might be important in explaining the underestimated velocity anomalies in the original traveltime tomography (Gao *et al.* 2004). Note a fast traveltime shift measured by a cross-correlation technique is healed slightly slower than a slow traveltime shift when the location of a velocity anomaly is close to the receiver. More importantly, because Gao *et al.* (2004) effectively picked the traveltime shift using the onset of a filtered body wave, it suggests a much less healing for a fast traveltime shift (Wielandt 1987) and explains the smaller amplification factor of fast anomalies (two times) used in our preferred model A.

As we have presented in this report, the broad-band waveform and amplitude variations recorded by the LA RISTRA transect provide invaluable constraints on the magnitude and geometry of the velocity structure in the mantle across the western Great Plains and the Rio Grande Rift. The slab-like fast anomaly presented by Gao *et al.* (2004) is validated and amplified according to our modelling result. As shown previously, we directly amplify the tomographic image and test it against waveform and amplitude data. Although this procedure is rather simple and it can certainly involve more delicate processes, we primarily target on how the traveltime tomographic images can be improved and validated through forward modelling waveforms and amplitudes.

If our model is correct, such a slab-like feature deserves more attention because it extends to nearly 600 km and is located right beneath the edge between the Rio Grande Rift and the western Great Plains where large variations in lithospheric thickness occur (Gao *et al.* 2004; West *et al.* 2004a,b) and small-scale convection might

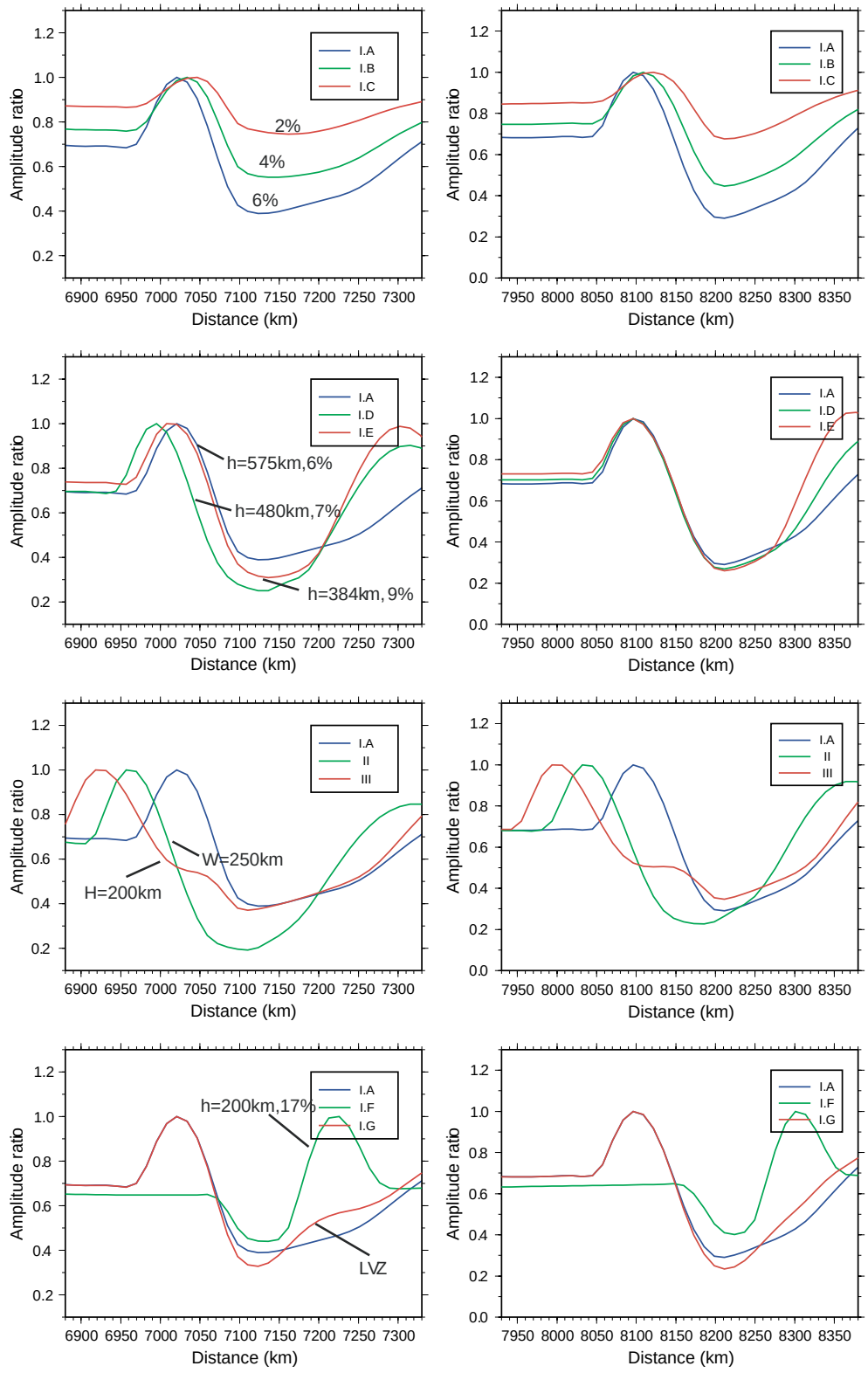

Figure 13. Sensitivity test of synthetic amplitude ratios against slab geometry. Left-hand panels show the result computed at shorter ranges (62°–66.5°) and right-hand panels show the result computed at longer ranges (71.5°–75°). The first row presents the comparisons of synthetic amplitude ratios against the velocity anomaly of the slab (model I.A, I.B and I.C). The second row presents comparisons of synthetic amplitude ratios against the depth of the slab (model I.A, I.D and I.E). The third row present comparisons of synthetic amplitude ratio against the dipping angle and the width of the slab (model I.A, II and III). The fourth row presents comparisons of synthetic amplitude ratios against the existence of the slab and low velocity zone (model I.A, I.F and I.G). See also Table 4.

Table 5. LA RISTRA slab parameters.

No.	*W* (km)	*H* (km)	*h* (km)	*X* (per cent)	LVZ	*Y* (km)
SD-1	120	120	575	6	no	6940
SD-2	170	120	575	3.75	no	6940
SD-3	100	120	380	4.5	no	6940
SD-4	140	120	575	4.5	no	6940

Table 6. Misfit of event 991130.

Model	SD-1	SD-2	SD-3	SD-4
Misfit-Time	3.759	1.845	1.909	2.385
Misfit-Amp	0.216	0.228	0.465	0.190

be important (King & Anderson 1998). However, there exists large difference between the original and amplified model in geophysical and dynamic inferences such as temperature, composition and buoyancy. We will discuss here in the context of the simplified model. Our model shows that the slab-like feature is about 4 per cent faster than the mantle beneath the Rio Grande Rift. Since we have to amplify the tomography model by a factor of 2–3 to fit the waveform and amplitudes, we assume that the slab-like anomaly imaged by the tomography is 2 per cent faster than the mantle beneath the Rio Grande Rift. Assuming temperature derivative $\partial \ln Vs/\partial T$ of -1 per cent/100 °C (Karato 1993), our model would predict temperature contrast across this anomaly of about 400 °C, whereas the tomographic model would suggest temperature contrast of 200 K only. If we assume thermal expansion coefficient α of $3 \times 10^{-5}\ C^{-1}$ (Fei 1995), we predict density change $\Delta\rho/\rho$ of 1.2 per cent, whereas the original model would suggest $\Delta\rho/\rho$ of 0.6 per cent. These differences certainly effect dynamic flow modelling where the mantle flow is driven by buoyancy.

In addition, the *P*-wave anomalies are much smaller than the *S*-wave anomalies in the original tomography model and the slab-like anomaly is almost invisible in the *P*-wave image (fig. 7 in Gao *et al.* 2004), which would suggest that temperature effect is probably dominant. However, the *P*-wave record section presented earlier also shows obvious waveform distortions and amplitude decays as seen in the *S*-wave section (Fig. 3). It is likely that compositional effects are also important in interpreting the slab-like anomaly. Although *S*-wave anomaly is very useful in inferring the temperature contrast (Karato 1993; Goes *et al.* 2000; Cammarano *et al.* 2003), however, it is difficult to infer the composition without other data such as *P*-wave anomalies (Niu *et al.* 2004; Song & Helmberger 2007) or gravity data (Forte & Perry 2000; Perry *et al.* 2003). If the slab-like anomaly was part of the continental lithosphere beneath the Great Plains, it would have probably been depleted (Jordan 1988; Lee 2003). In this case, the net buoyancy of this slab-like feature has to be reevaluated and it is not clear whether this slab-like anomaly mapped in the original tomographic model can indeed sink as proposed because it depends on the buoyancy, viscosity and strength of the lithosphere, which are strongly temperature-dependent (Lenardic & Moresi 1999; Lenardic *et al.* 2003). We will not discuss this issue further without analysing *P*-wave data while the main issue here is to demonstrate the usefulness of using waveforms and amplitude information in validating tomographic models.

In this study, we have found that the use of waveform diffraction and amplitude pattern increases the velocity contrast across the Rio Grande Rift and the western Great Plains, which has both geodynamic and geochemical implications. It is not surprised that waveform and amplitude data can provide an independent constraint on the velocity gradient (Nowack & Lutter 1988; Bostock & VanDecar 1994) and they are very complementary to traveltime data that are sensitive to the bulk velocity perturbation. Neele *et al.* (1993) have suggested that amplitude data would serve as a great validation tool for traveltime tomography and it is successfully demonstrated in our analysis. As a ray-based tomography evolves to a more advanced finite-frequency tomography (Dahlen *et al.* 2000), its resolving power and model improvement relative to a ray-based tomography (Montelli *et al.* 2006; Van der Hilst & de Hoop 2006) certainly can be justified and validated using amplitude and waveform data through forward modelling. Finally, resolving the shallow mantle structure can greatly improve the resolution of deep mantle structure and avoid mistakeningly mapping shallow heterogeneities into complex deep features (Weber 1994).

6 CONCLUSIONS

In summary, we have presented a systematic analysis of the use of waveform and amplitude information in exploring the slab-like structure beneath the eastern edge of the Rio Grande Rift in the southwestern United States. Broad-band waveform from South American events recorded by the LA RISTRA transect clearly show systematic amplitude decays across the slab-like feature imaged

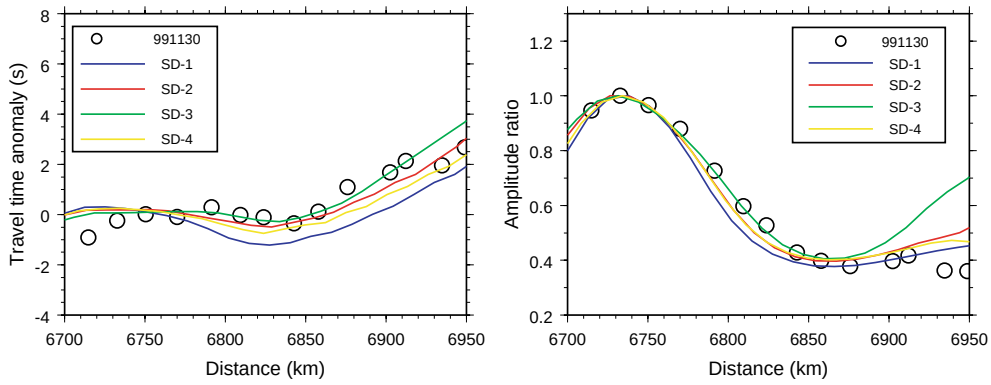

Figure 14. Modelling slab geometry under LA RISTRA transect. Top panel shows the geometry of the slab that mimics the *S*-wave tomographic image by Gao *et al.* (2004) and explains the observed traveltime delays and amplitude ratios for event 991130 (See also Table 5). Bottom panels show FD synthetic traveltime delays and amplitude ratios for model SD-1, SD-2, SD-3 and SD-4. Model SD-1 explains the observed amplitude ratios reasonably well but the predicted traveltime is systematic too early. Model SD-3 explains the observed traveltime delay but fails to predict the amplitude ratios correctly. Model SD-2 and SD-3 are able to explain the observed amplitude ratios as well as traveltime delays.

by the traveltime tomography (Gao *et al.* 2004). These waveforms demonstrate clear multipathing phenomena supported by finite difference simulations where incoming teleseismic wavefronts are distorted by the slab feature beneath the receivers. In general, the slab-like anomaly has to be amplified about two to three times to explain the waveform distortion at stations near the transition from the western Great Plains and the Rio Grande Rift. We performed sensitivity tests and found that the amplitude information can be utilized with the traveltime delays to better determine the slab geometry. Our preferred model has a fast slab (3.8–4.5 per cent) with thickness of 120 km dipping 70°–75° to the southeast to nearly 600 km and is consistent with both traveltime and amplitude observations. We believe that amplitude systematics and waveform distortions can provide additional and tighter constraints on the geometry and magnitude of seismic anomalies, which would improve inferences on their origins.

ACKNOWLEDGMENTS

The authors would like to thank Don Anderson for reviewing an early version of this paper and John VanDecar for pointing out early work on amplitude data. In particular, we appreciate comments from the editor Thorsten Becker, James Ni and an anonymous reviewer, which substantially improve and clarify this paper. This work was supported by the National Science Foundation, Grant # EAR−0639507 and contribution no. 9173 of the Division of Geological and Planetary Sciences, California Institute of Technology.

REFERENCES

Achauer, U. & Masson, F., 2002. Seismic tomography of continental rifts revisited: from relative to absolute heterogeneities, *Tectonophysics*, **358,** 17–37.

Baldridge, W.S. *et al.*, 1991. Middle to late Cenozoic magmatism of the southeastern Colorado Plateau and central Rio Grande Rift (New Mexico and Arizona, USA): a model for continental rifting, *Tectonophysics*, **197,** 327–354.

Bostock, M.G. & VanDecar, J.C., 1994. The influence of crust and upper-mantle heterogeneity on short-period waveform distortion, *Phys. Earth Planet. Inter.,* **83,** 225–247.

Bostock, M.G., VanDecar, J.C. & Sneider, R., 1993. Modeling teleseismic P-wave propagation in the upper mantle using a parabolic approximation, *Bull. Seism. Soc. Am.,* **83,** 756–779.

Cammarano, F., Goes, S., Vacher, P. & Giardini, D., 2003. Inferring upper-mantle temperatures from seismic velocities, *Phys. Earth Planet. Inter.,* **138,** 197–222.

Cormier, V.F., 1989. Slab diffraction of *S* waves, *J. Geophys. Res.*, **94,** 3006–3024.

Dahlen, F.A., Hung, S.-H. & Nolet, G., 2000. Frechet kernels for finite-frequency traveltimes, I., Theory, *Geophys. J. Int.,* **141,** 157–174.

Davis, P.M. & Slack, P.D., 2002. The upper mantle beneath the Kenya dome and relation to melting, rifting and uplift in East Africa, *Geophys. Res. Lett.,* **29,** doi:10.1029/2001GL013676.

Fei, Y., 1995. Thermal expansion, in *A Handbook of Physical Constants, Mineral Physics and Crystallography,*Vol. 2, pp. 29–44, American Geophysical Union.

Forte, A.M. & Perry, H.K.C., 2000. Geodynamics evidence for a chemically depleted continental tectosphere, *Science,* **290,** 1940–1944.

Gao, S.S., Liu, K.H., Davis, P.M., Slack, P.D., Zorin, Y.A., Mordvinova, V.V. & Kozhevnikov, V.M., 2003. Evidence for small-scale mantle convection in the upper mantle beneath the Baikal rift zone, *J. Geophys. Res.*, **108,** doi:10.1029/2002JB002039.

Gao, W., Grand, S., Baldridge, W.S., Wilson, D., West, M., Ni, J. & Aster, R., 2004. Upper mantle convection beneath the central Rio Grande rift imaged by *P* and *S* wave tomography, *J. Geophys. Res.*, **109,** doi:10.1029/2003JB002743.

Godey, S., Deschamps, F., Trampert, J. & Snieder, R., 2004. Thermal and compositional anomalies beneath the North American continent, *J. Geophys. Res.*, **109,** doi:10.1029/2002JB002263.

Goes, S., Govers, R. & Vacher, P., 2000. Shallow mantle temperatures under Europe from *P* and *S* wave tomography, *J. Geophys. Res.*, **105,** 11 153–11 169.

Grand, S. & Helmberger, D.V., 1984. Upper mantle shear structure of North America, *Geophys. J. R. Astro. Soc.*, **76,** 399–438.

Grand, S.P., 2002. Mantle shear-wave tomography and the fate of subducted slabs, *Phil. Trans. R. Soc. London, Ser. A,* **360,** 2475–2491.

Hammond, W.C. & Humpreys, E.D., 2000. Upper mantle seismic wave velocity: effects of realistic partial melt geometries, *J. Geophys. Res.*, **105,** 10 975–10 986.

Helmberger, D. & Ni, S., 2005. Approximate 3D body-wave synthetics for tomographic models, *Bull. Seism. Soc. Am.*, **95,** 212–224.

Helmberger, D. & Vidale, J., 1988. Modeling strong motion produced by earthquakes with two-dimensional numerical codes, *Bull. Seism. Soc. Am.*, **78,** 109–121.

Hung, S.-H., Dahlen, F.A. & Nolet, G., 2001. Wavefont healing: a banana-doughnut perspective, *Geophys. J. Int.*, **146,** 289–312.

Jain, A.K., 1989. *Fundamentals of Digital Image Processing, Prentice Hall Information and System Sciences Series*, Prentice Hall, NJ.

Jordan, T.H., 1988. Structure and formation of the continental tectosphere, *J. Petro.* Special Issue, 11–37.

Karato, S.I., 1993. Importance of anelasticity in the interpretation of seismic tomography, *Geophys. Res. Lett.,* **20,** 1623–1626.

King, S.D. & Anderson, D., 1998. Edge-driven convection, *Tectonophysics*, **160,** 289–296.

Lee, C.-T.A., 2003. Compisitional variation of density and seismic velocities in natural peridotites at STP conditions: implications for seismic imaging of compisitional heterogeneities in the upper mantle, *J. Geophys. Res.*, **108,** doi:10.1029/2003JB2413.

Lenardic, A. & Moresi, L.N., 1999. Some thoughts on the stability of cratonic lithosphere: effects of buoyancy and viscosity, *J. Geophys. Res.*, **104,** 12 747–12 758.

Lenardic, A., Moresi, L.N. & Muhlhaus, H., 2003. Longevity and stability of cratonic lithosphere: insights from numerical simulations of coupled mantle convection, *J. Geophys. Res.*, **108,** doi:10.1029/2002JB001859.

Montelli, R., Nolet, G. & Dahlen, F.A., 2006. Comment on 'banana-doughnut kernels and mantle tomography' by van der hilst and de hoop, *Geophys. J. Int.*, **167,** 1204–1210.

Myers, S.C., Beck, S., Zandt, G. & Wallace, T., 1998. Lithospheric-scale structure across the Bolivian Andes from tomographic images of velocity and attenuation for *P* and *S* waves, *J. Geophys. Res.*, **103,** 21 233–21 252.

Neele, F., VanDecar, J.C. & Snieder, R., 1993. The use of *P* wave amplitude data in a joint inversion with traveltimes for upper mantle velocity structure, *J. Geophys. Res.*, **98,** 12 033–12 054.

Ni, S., Helmberger, D.V. & Tromp, J., 2005. Three-dimensional structure of the African superplume from waveform modeling, *Geophys. J. Int.*, **161,** 283–294.

Niu, F., Levander, A., Cooper, C.M., Lee, C.-T.A., Lenardic, A. & James, D.E., 2004. Seismic constraints on the depth and composition of the mantle keel beneath the Kaapvaal craton, *Earth Planet. Sci. Lett.*, **224,** 337–346.

Nowack, R.L. & Lutter, W.J., 1988. Linearized rays, amplitude and inversion, *Pure Appl. Geophys.*, **128,** 401–421.

Perrot, J., Deschamps, A., Farra, V. & Virieux, V., 1994. Azimuthal distortion of the seismic focal sphere - application to earthquakes in subduction, *Phys. Earth Planet. Inter.*, **84,** 247–270.

Perry, H.K.C., Forte, A.M. & Eaton, D.W.S., 2003. Upper-mantle thermochemical structure below North America from seismic-geodynamic flow models, *Geophys. J. Int.*, **154,** 279–299.

Roth, E.G., Wiens, D.A., Dorman, L.M., Hildebrand, J. & Webb, S.C., 1999. Seismic attenuation tomography of the Tonga-Fiji region using phase pair method, *J. Geophys. Res.*, **104,** 4795–4809.

Sekiguchi, S., 1992. Amplitude distribution of seismic waves for laterally heterogeneous structures including a subducting slab, *Geophys. J. Int.*, **111,** 448–464.

Slack, P.D., Davis, P.M., Dahlhei, M., Glaha, A., Ritter, J.R.R., Green, W.V., Maguire, P.K.H. & Meyer, R.P., 1994. Attenuation and velocity of *P*-waves in the mantle beneath the east-African rift, Kenya, *Tectonophysics*, **236,** 331–358.

Slack, P.D., Davis, P.M., Baldridge, W.S., Olson, K.H., Glahn, A., Achauer, U. & Spence, W., 1996. The upper mantle structure of the central Rio Grande Rift region from teleseismic *P* and *S* wave traveltime delays and attenuations, *J. Geophys. Res.*, **101,** 16 003–16 023.

Song, T.-R.A., 2006. Broadband modeling of earthquake sources and mantle structures, *PhD thesis*, California Institute of Technology.

Song, T.-R.A. & Helmberger, D.V., 2006. Low velocity zone atop the transition zone in the western us from s waveform triplications, in *Earth's Deep Water Cycle, Geophysical Monograph,*Vol. 168, pp. 195–213, eds Jacobsen, S.D. & Van der Lee, S., American Geophysica Union.

Song, T.-R.A. & Helmberger, D.V., 2007. *P* and *S* waveform modeling of continental sub-lithospheric detachment at the eastern edge of the Rio Grande Rift, *J. Geophys. Res.*, in press.

Song, T.-R.A., Sun, D.-Y. & Helmberger, D.V., 2005. 2-D finite difference modeling of the D″ structure beneath the eastern Cocos plate: Part I, *Eos Trans. AGU,* 86(52), Fall Meet. Suppl., Abstract S34C-05.

Takei, Y., 2000. Acoustic properties of partially molton media studied on a simple bindary system with a controllable dihedral angle, *J. Geophys. Res.*, **105,** 16 665–16 682.

Tiberi, C., Diament, M., Deverchere, J., Petit-Mariani, C., Mikhailov, V., Tikhotsky, S. & Achauer, U., 2003. Deep structure of the Baikal rift zone revealed by joint inversion of gravity and seismology, *J. Geophys. Res.*, **108,** doi:10.1029/2002JB001880.

Van der Hilst, R.D. & de Hoop, M.V., 2006. Reply to comment by Montelli, R., Nolet, G. & Dahlen on, F.A., 'Banana-doughnut kernels and mantle tomography', *J. Geophys. Res.*, **167,** 1211–1214.

Vidale, J.E., 1987. Waveform effect of a high-velocity, subducted slab, *Geophys. Res. Lett.*, **14,** 542–545.

Vidale, J., 1988. Finite-difference calculation of travel-times, *Bull. Seism. Soc. Am.*, **78,** 2062–2076.

Vidale, J., Helmberger, D.V. & Clayton, R.W., 1985. Finite difference seismograms for *SH* waves, *Bull. Seism. Soc. Am.*, **75,** 1765–1782.

Wang, Y. & Wen, L., 2004. Mapping the geometry and geographic distribution of a very low velocity province at the base of the Earth's mantle, *J. Geophys. Res.*, **109,** doi:10.1029/2003JB002674.

Weber, M., 1990. Subduction zones - their influence on traveltimes and amplitudes of *P*-waves, *Geophys. J. Int.*, **101,** 529–544.

Weber, M., 1994. Traveltime and amplitude anomalies at the seismic broadband array grf, *Geophys. J. Int.*, **118,** 57–74.

West, M., Gao, W. & Grand, S., 2004a. A simple approach to the joint inversion of seismic body and surface waves applied to the southwest US, *Geophys. Res. Lett.*, **31,** doi:10.1029/2004GL020373.

West, M., Ni, J., Baldridge, W.S., Wilson, D., Aster, R., Gao, W. & Grand, S., 2004b. Crust and upper mantle shear wave structure of the southwest United States: implications for rifting and support for high elevation, *J. Geophys. Res.*, **109,** doi:10.1029/2003JB002575.

Wielandt, E., 1987. On the validity of the ray approximation for interpreting delay times, in *Seismic Tomography*, pp. 85–98, ed. Nolet, G., Dordrecht, Reidel.

Wilson, D., Leon, J., Aster, R., Ni, J., Grand, S., Semken, S., Gao, W. & Baldridge, W.S., 2002. Broadband seismic background noise at temporary seismic stations observed on a regional scale in the southwestern United States, *Bull. Seism. Soc. Am.*, **92,** 3335–3341.

Wilson, D., Aster, R., Ni, J., Grand, S., West, M., Gao, W., Baldridge, W.S. & Semken, S., 2005a. Imaging the seismic structure of the crust and upper mantle beneath the Great Plains, Rio Grande Rift, and Colorado Plateau using receiver functions, *J. Geophys. Res.*, **110,** doi:10.1029/2004JB003492.

Wilson, D., Aster, R., West, M., Ni, J., Grand, S., Gao, W., Baldridge, W.S. & Semken, S., 2005b. Lithospheric structure of the Rio Grande Rift, *Nature,* **433,** 851–855.

Zhou, H.W. & Chen, G.M., 1995. Waveform response to the morphology of 2-D suducted slab, *Geophys. J. Int.*, **121,** 511–522.